Automatic Working Area Classification in Peripheral Blood Smears

Wei Xiong, S.H. Ong, Joo-Hwee Lim, Kelvin Foong Weng Chiong, Jiang Liu, Daniel Racoceanu, Alvin G. L. Chong, Kevin S. W. Tan

Automatic Area Classification in Peripheral Blood Smears

Wei Xiong*, *Member, IEEE*, S. H. Ong, *Member, IEEE*, Joo-Hwee Lim, *Member, IEEE*, Kelvin Foong Weng Chiong, Jiang Liu, Daniel Racoceanu, *Member, IEEE*, Alvin G. L. Chong, and Kevin S. W. Tan

***Abstract*—Cell enumeration and diagnosis using peripheral blood smears are routine tasks in many biological and pathological examinations. Not every area in the smear is appropriate for such tasks due to severe cell clumping or sparsity. Manual working area selection is slow, subjective, inconsistent and statistically biased. Automatic working area classification can reproducibly identify appropriate working smear areas. However, very little research has been reported in the literature. With the aim of providing a preprocessing step for further detailed cell enumeration and diagnosis for high throughput screening, we propose an integrated algorithm for area classification and quantify both cell spreading and cell clumping in terms of individual clumps and the occurrence probabilities of the group of clumps over the image. Comprehensive comparisons are presented to compare the effect of these quantifications and their combinations. Our experiments using images of Giemsa-stained blood smears show that the method is efficient, accurate (above 88.9% hit rates for all areas in the validation set of 140 images) and robust (above 78.1% hit rates for a test set of 4878 images). This lays a good foundation for fast working area selection in high throughput screening.**

***Index Terms*—Peripheral blood smear, working area, clumping, classification, high throughput screening**

I. Introduction

PERIPHERAL blood smears are widely used in biological and pathological examinations. Blood smear preparation requires the dropping of a blood sample on a glass slide, spreading the sample and staining. Sample spreading is done by pulling a wedge to spread a drop of blood sample on the slide. This produces a gradual decrease in thickness of the blood from the thick to the thin end with the smear terminating in a feathered edge [1]. At the thick end, most of the cells are clumped, which increases the difficulty in identifying and analyzing blood components. The smear gradually becomes thinner towards the other end. Finally the cells distribute unevenly, and grainy streaks, troughs, ridges, waves or holes may be present. This portion of the smear has insufficient useful information for analysis. A section with a monolayer of cells is located somewhere between the two ends. The thickness of the smear is influenced by the angle of the spreader (the wedge), the size of the drop of blood and the speed of spreading. The appearance (color, shape and texture) of stained smears under the microscope depends on factors such as the concentration of stains, presence of anti-coagulants, lighting, exposure, artifacts, and so on. According to domain experts, the areas in the smears can be categorized into three classes in terms of cell spreading and morphology, namely, clumped, good, and sparse, denoted by "C", "G" and "S", respectively. Fig. 1 shows typical images captured from these three areas.

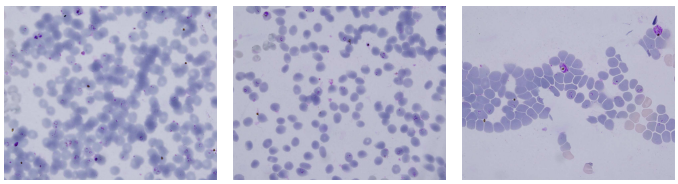

(a) (b) (c)

Fig. 1. Typical areas: (a) clumped, (b) good, and (c) sparse.

In current laboratory practice, skilled users manually identify *good working areas* (GWAs) to acquire images for enumeration, diagnosis, storing, transmitting and processing. By GWAs, we refer to those areas having a high density of well-separated cells with acceptable morphology. Due to the aforementioned reasons, GWAs vary in morphology and specific appearances in different slides. At the time of inspection, a decision has to be made as to where to start the examination [2]. Such manual identification is tedious, inconsistent and prone to error, and is also biased in terms of statistics and user subjectivity. Automatic GWA detection is desirable since it can increase consistency, reduce labor, and achieve better accuracy.

Advances in high-throughput microscopy have enabled the

*W. Xiong is with the Institute for Infocomm Research (I2R), Agency for Science Technology and Research (A*STAR), and the Image and Pervasive Access Laboratory (IPAL) (UMI 2955, French National Center for Scientific Research), Singapore 138632 (email: wxiong@i2r.a-star.edu.sg).

S.-H. Ong is with the Department of Electrical and Computer Engineering, National University of Singapore, Singapore 117576 (email: eleongsh@nus.edu.sg).

J.-H. Lim is with the Institute for Infocomm Research (I2R), Agency for Science Technology and Research (A*STAR), and the Image and Pervasive Access Laboratory (IPAL) (UMI 2955, French National Center for Scientific Research), Singapore 138632 (email: joohwee@i2r.a-star.edu.sg).

K.W.C. Foong is with the Faculty of Dentistry, National University of Singapore, Singapore 119083 (email: kelvinfoong@nuhs.edu.sg).

J. Liu is with the Institute for Infocomm Research, Agency for Science Technology and Research (A*STAR), Singapore 138632 (email: jliu@i2r.a-star.edu.sg).

D. Racoceanu is with the French National Center for Scientific Research and the Image and Pervasive Access Laboratory (IPAL) (UMI 2955, French National Center for Scientific Research), Singapore 138632 (e-mail: daniel.racoceanu@ens2m.fr).

A. G. L. Chong and K. S. W. Tan are with the Department of Microbiology, National University of Singapore, Singapore 117597 (email: miccgla@nus.edu.sg; mictank@nus.edu.sg).

rapid acquisition of many images (of the order of 10^4) without human intervention for the purpose of large-scale screening, i.e., high-throughput screening (HTS) [3]. Depending on the sample size on the slide, one could easily acquire more than ten thousand images, each containing a few hundred cells using a $100\times$ objective. Manual counting is impractical as it will take about one week to count the cells in just one slide assuming a rate of one minute per image. It would be much faster to first automatically obtain the GWAs followed by counting cells within these areas. Hence, in the context of HTS and telepathology applications [4], automatic GWA detection is necessary as a preprocessing step for large-scale cell counting.

Despite its importance, automatic GWA detection has been rarely investigated compared to studies on automatic blood cell classification [5]. To our knowledge, there are only two relevant papers in this field published by others, in 1987 [2] and 2003 [6]. Reference [2] is a patent that describes the measurement of areas and perimeters of cell regions by incorporating *ad hoc* conditions. The method considers a region a GWA if the ratio η of the total area to the total perimeter is less than a fixed threshold. It is claimed that this parameter can be used to discriminate GWAs from those areas that are *too densely* or *too sparsely* populated with red blood cells. However, validation of the results was not provided.

Reference [6] presents a method for quick detection of well-spread areas in smears under low magnification ($16\times$ or $25\times$ objective). The algorithm first extracts the red blood cells (RBCs), the centers of the cells, and the *cells with centers*. Although the term "cells with centers" is not explicitly defined in [6], it is clear that the work relies on the extraction of the so-called *pale-staining central zones* (PCZs) in cells caused by their biconcavity [7]. Such PCZs are only observable in some cells in Giemsa-stained smears without coverslips (Fig. 1(b) and Fig. 1(c)). For the purpose of long-term preservation, smears are covered by coverslips, in which case, the cells appear flat and biconcavity is seldom observed [8]. In [6], the number of connected components from the three kinds of particles are counted for calculating the coefficient of cell spreading and the coefficient of cell overlapping. If the coefficients are greater than 0.50 and 0.73, respectively, the area is considered a GWA. However, both numbers are set empirically, and hence not optimal.

In view of the above, we have recently reported an approach [8] that measures GWAs without cell center extraction and thus does not rely on PCZs. Instead, we employ two generic global features in the image, namely, the average occupancy of connected components α, and the average equivalent diameter β. A cascading classification approach is proposed to detect GWAs. The essential parts are two thresholding methods whose parameters are determined by some intuitive rules followed by leave-one-out cross-validation. Based on the features η, α and β, we achieved promising results.

A pyramid image representation is adopted in [9] to describe feature spatial distributions and to measure the feature homogeneity by using the feature percentages and their standard derivation σ at each pyramid level. The selection of appropriate features and *quantitative* image classification are not discussed. We have applied the pyramid representation in [10] to detect GWAs, where we also propose two new across-scale measures.

A particular difficulty in automatic cell image processing is to separate cell clumps into individual cells. The manner in which cells aggregate influences the efficacy of automatic separation. It is relatively simpler to split two touching cells than two heavily overlapped cells, and also to separate a two-cell clump than a multiple-cell clump.

In this work, we propose to measure, for an object, its degree of cell clumping in terms of both its area and the number of cells it contains. The object area (relative to the area of a normal (i.e., healthy) cell) can be regarded as a measure of the degree of cell overlap for *individual* objects. In "C" images, some objects are significantly larger than others, while in "G" images, the variation in object sizes is relatively moderate. We can discriminate between these images by computing the Shannon entropy from the area probability distribution of all the objects in each image. In order to deliver efficient GWA detection and area classification in the context of HTS, it would be preferable that these measurements are computationally undemanding. Hence, we adopt a simple, yet efficient and accurate, cell-splitting approach that is aimed at image area classification instead of accurate cell segmentation. We select appropriate features for the classification task and validate our approaches using comprehensive experiments on large datasets.

The major contributions of this paper are: 1) an integrated algorithm to classify a large set of blood smear images into good, clumped and sparse regions for the purpose of identifying GWAs, 2) a method that considers both feature spatial distribution and cell clumping for GWA detection, and 3) optimal feature selection for image classification.

The rest of the paper is organized as follows. Sections II and III describe the methods for image analysis and feature extraction. We explain the classification algorithm in Section IV. Section V presents the experimental results and discussion, followed by the conclusion in the final section.

II. Image analysis and clump characterization

A. Image analysis

Our approach to GWA detection requires the quantification of cell clumping and spreading. To measure the former, we need to know the number of cells that are clumped together to form a connected component (called an *object* here). Knowing the total number of cells and the total number of objects in the image is also useful. For cell spreading, the variance of the number of cells in local regions is an indication of cell spreading homogeneity. To obtain these features, we analyze the images in four steps:

1) image preprocessing;
2) connected component labeling;
3) clump splitting and cell counting;
4) feature extraction.

The color images (of size 1280×1024 pixels) in our experiments are acquired from malaria-infected Giemsa-stained

blood smears (with covers) using an oil immersion $100\times$ objective and a $10\times$ ocular. The image is first represented in hue-saturation-value (HSV) color space. To reduce the influence of color changes due to variations in source illumination and camera exposure, we process its value channel. The image shown in Fig. 1(b) is used to illustrate the processing steps. In this figure, the red blood cells appear dimmer than the plasma (background). For the ease of manipulation, the inverse of this channel is obtained to make the cells appear brighter than the background. Median filtering is then applied to remove noise. The gray level histogram (Fig. 2(a)) of the resulting image, $g(x, y)$, is bimodal, with the brighter mode comprising the RBCs whose morphology and distribution are our prime concern.

Otsu's method [11] is a widely-used thresholding method. Although it is a global method, it is fairly robust to different illumination and color changes and works well for our images. Morphological image processing is then applied to separate the objects and remove isolated pixels. The resulting binary image is denoted by $g_1(x, y)$ (Fig. 2(b)). Note that each image may contain n_b objects and each object i, $i = 1, ..., n_b$, may contain m cells. For the n_b objects in the image, the region properties of each object i, including area $a(i)$ and perimeter $c(i)$, are found. Further, we have $\eta = \sum_{i=1}^{n_b} a(i) / \sum_{i=1}^{n_b} c(i)$.

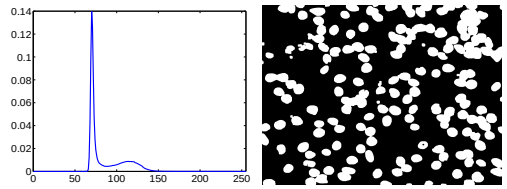

(a) (b)

Fig. 2. (a) Histogram of the gray image $g(x, y)$, and (b) $g_1(x, y)$.

B. An efficient clump-splitting method

In this subsection, we describe how clumped objects are split into individual cells. There are four major clump-splitting approaches: binary erosion [12], watershed [13], model-based [14] and concavity analysis [15]–[17]. Erosion-based methods face difficulties in choosing suitable mask sizes for erosion, and consequently a constituent object may be completely eroded before a split occurs. The watershed algorithm splits an image into areas according to the topology of the image. During the flooding of an inverted distance-transformed image (if the original image is binary) or a gray level relief (if the original image is gray-valued), watersheds with adjacent catchment basins are constructed [18]. Watershed techniques tend to over-split the clumps and generate false splitting. Model-based approaches [14], [19], [20] require proper initialization of the model parameters [20] and are usually costly to compute. Concavity analysis methods [16], [17] are based on shape alone and depend on subjective rules to decide where to split clumps. In addition, if there is severe cell overlap, the shape outline may not be sufficient to determine splitting lines and the clumps may not be split at all.

In our application, automatic area classification is a preprocessing step before further accurate and detailed cell enumeration and analysis. Note that, since the number of images is large, any time-consuming approach might be inappropriate. Hence, we require, for this step, a clump-splitting algorithm that emphasizes speed with acceptable accuracy in GWA selection instead of more accurate but slow cell counting. We achieve this by combining image erosion and a modified watershed technique.

Morphological opening is first applied to $g_1(x, y)$ using a disk-shaped structuring element with radius u. This removes regions having a radius less than u and yields $f(x, y)$ (Fig. 3(a)). This is followed by a clump-splitting algorithm that works in transform space. First, we obtain $f_c(x, y)$, which is the complement of $f(x, y)$. Then we compute the Euclidean distance transform of $f_c(x, y)$. For each pixel in $f_c(x, y)$, the distance transform assigns a number that is the distance between that pixel and the nearest nonzero pixel of $f_c(x, y)$. The resulting image is a gray value image $f_d(x, y)$ (Fig. 3(b)). In naive watershed techniques, the zero-distance pixels are extracted from $f_d(x, y)$ to form splitting lines, which may yield many false partitions.

Since we do not have to find a complete splitting of cells or their exact boundaries, we apply an extended H-maxima transform [21] on $f_d(x, y)$ with parameter h to obtain a binary image $f_h(x, y)$ (Fig. 3(c)). This transform finds the regional maxima and suppresses those external boundary pixels whose distances from object boundaries are below h, thus separating the connected components.

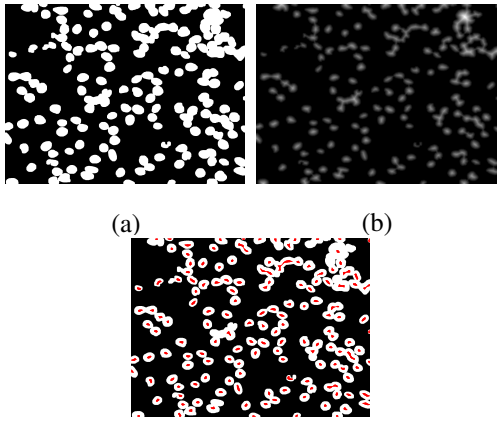

(a) (b)

(c)

Fig. 3. Splitting results: (a) $f(x, y)$, (b) $f_d(x, y)$, and (c) the split cells (in red) $f_h(x, y)$ overlaid on $f(x, y)$.

The parameters u and h require fine tuning so that, ideally, n-cell clumped regions will be separated into n isolated regions exactly and there is a one-to-one mapping between each isolated region and each cell identity. To achieve this, the cell dimensions, such as the semi-major axis length, a_l, and the semi-minor axis length, a_s, from *healthy* and separated *single* cells are obtained. The mean and the standard deviation of a_l (a_s) are denoted by $\overline{a_l}$ ($\overline{a_s}$) and $\widetilde{a_l}$ ($\widetilde{a_s}$), respectively. We obtain $\overline{a_s} = 27.4$, $\overline{a_l} = 35.0$, $\widetilde{a_s} = 3.2$ and $\widetilde{a_l} = 5.3$, all in pixels. The minimum value of a_s of single *healthy* RBCs

is about 17 pixels. Our aim is to separate two cells with an overlap of half a cell body. In this case, the distance between the two cell centers is the diameter. Thus we choose $h < 17$ pixels. For u, it should not be larger than the minimum of a_s as well, i.e., $u < 17$ pixels, so that no cell is removed. In our experiments we have conservatively chosen $h = 5$ and $u = 10$ pixels. The purpose for the margins in both h and u is to cope with possible over-segmentation in pathological and other regions as well as partial cells.

In Fig. 3, we observe that we can successfully split most clumps but fail in a small percentage of severely overlapped clumps. We also note that several cells are broken into multiple isolated fragments due to over segmentation. To avoid over-estimation, the isolated regions with very small areas should be removed. The centroid of each isolated region in $f_h(x, y)$ is finally used to count the number of cells in each object in $f(x, y)$. By labeling these regions in $f_h(x, y)$ we can find the number of cells within each object, and the total number of cells in $f(x, y)$.

Finally, we compute the entropy $e = -\sum p_A \log p_A$ to measure the cell clumping in the image collectively. Here p_A is the probability distribution function of all object areas within the image.

III. Characterizing Spatial Distribution of Features

We note that cells are spread unevenly towards the feathered edges in blood smears. Hence, measuring cell spatial distribution should be useful for GWA detection. Methods in the literature characterizing the spatial distribution of features fall into two categories depending on whether or not individual feature measurements are required [9]. Reference [22] extracts the spatial coordinates of the centroids of the features. For each feature, its nearest-neighbor feature is obtained. The distribution of these nearest neighbor distances can be used to measure feature spatial distribution. Finding such a distribution is computationally expensive.

Variations in feature spatial distribution can be directly characterized by *homogeneity* or *inhomogeneity* [9]. A discrete, as opposed to a continuous, homogeneity status is not sufficiently fine to incorporate other continuous features for working area classification. In image processing, color variance, kurtosis [23], and entropy [24] have been used to measure homogeneity. We have chosen to use the standard deviation derived from an image pyramid representation [9], [10].

At each level of the pyramid, an image is partitioned into four quadrants (two in each dimension). This partitions the image hierarchically from the lowest (i.e., coarsest) scale ($k = 0$, without partitioning) to the highest (i.e., finest) scale ($k = K$), resulting in $q_k = 4^k$ blocks (child regions) at level k, $k = 0, \ldots, K$. For each k, we define the spatial occupancy α_j^k of a feature in the jth block B_j^k, $j = 1, \ldots, q_k$, as $\alpha_j^k = \sum_x \sum_y f(x, y)/|B_j^k|$, where $|B_j^k|$ is the area of B_j^k and the summations are over all pixels (x, y) in the block and $f(x, y)$ is 1 if pixel (x, y) belongs to a cell, and 0 otherwise. Of all α_j^k at each level k, their mean value, $\mu_k = \sum_{i=1}^{q_k} \alpha_j^k / q_k$, and their standard derivation value,

$$\sigma_k = \sqrt{\sum_{i=1}^{q_k} (\alpha_j^k - \mu_k)^2 / (q_k - 1)} \tag{1}$$

are calculated. At level $k = 0$, $\sigma_0 = 0$ as there is only one block. Hence σ_0 is not used here. For different scales, μ_k but are almost the same [9] and thus can be treated as a single feature. Let us denote it by $\alpha = \mu_0$, which is the occupancy in the entire image. Note that α is proportional to $\sum_{i=1}^{n_b} a(i)$ and hence it is a measure of cell overlap. σ_k is related to the scale of observation (i.e., the block size), the object sizes and their spatial organization (for example, whether objects are distributed uniformly or concentrate at certain parts of the image) [9]. To illustrate this, Fig. 4 shows three $\sigma_k \sim k$ curves for the three images shown in Fig. 1.

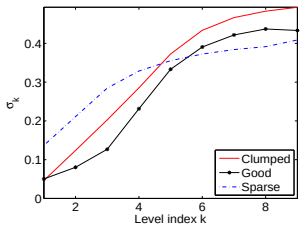

Fig. 4. Standard derivations (vertical axis) at different pyramid levels (horizontal axis).

The differences among the curves are obvious, indicating that σ_k can be used to encode spatial distributions. The general shapes of the curves may be explained as follows. In our experiments, the image size is 1024×1280 pixels and the average dimension of normal cells is about 54×70 pixels. In the pyramid representation, the block sizes at levels $k = 4, 5, 6$ are 64×80, 32×40 and 16×20 pixels, respectively. The block size at level 5 is closest to a normal cell size. At coarse levels $k = 1, 2, 3$, where the block sizes are large, the blocks are likely to contain entire cells. Since objects in "S" images tend to concentrate at certain parts of the image (see Fig. 1(c)), there is a high chance that some blocks contain cells while others do not. Hence the variation in the spatial occupancies in these blocks tends to be larger than those in "C" and "G" images. At finer levels ($k = 7, 8, 9$), the blocks are small and are more likely to contain parts of cells or parts of clumps in "C" and "G" images as the sizes of these objects in these images tend to be larger than the blocks. Since there are large variations in the object parts which are contained in the blocks, the occupancies of the blocks vary, and hence the occupancy variances in "C" and "G" images tend to be larger than those in "S" images at finer levels.

This analysis shows that σ_k at coarse or fine levels can be used to classify the three types of images. In fact, we can use σ_k both individually (a single σ_k at a certain k) and collectively. For the former, we will select the optimum through experiments. For the latter, we define the spatial homogeneity of $f(x, y)$ as the mean value of σ_k across scales [10]: $\lambda = \sum_{k=1}^{K} \sigma_k^2 / K$. We also observe that the "G"

image has a lower value of area under its curve. Hence, we include the area $\tau = \sum_{k=1}^{K} \sigma_k$ as a new feature.

IV. Classification Methodology

We can employ supervised classification methods using support vector machines (SVMs). Given training samples $\{(x_i, z_i)\}$, $x \in \mathrm{R}^m$, $z_i \in \{-1, 1\}$, $i = 1, \ldots, N$, the two-class soft SVM is to find Lagrange multipliers $\xi = \{\xi_i\}_{i=1}^{N}$ such that [25]

$$J(\xi) = \sum_{i=1}^{N} \xi_i - \frac{1}{2} \sum_{i=1}^{N} \sum_{j=1}^{N} \xi_i \xi_j z_i z_j \phi(x_i, x_j) \tag{2}$$

is maximized subject to

$$\sum_{i=1}^{N} \xi_i z_i = 0, \quad 0 \le \xi_i \le C. \tag{3}$$

Here C is the control parameter and $\phi(x_i, x_j)$ the kernel. We take the linear kernel $\phi(x_i, x_j) = x_i^T x_j$ for simplicity. We let $\hat{\xi} = \left\{\hat{\xi}_i\right\}_{i=1}^{N}$ and $b = b(\hat{\xi})$ be the optimal parameters such that $f(x) = 0$ is the class boundary with

$$f(x) = \sum_{i=1}^{N} \hat{\xi}_i z_i k(x, x_i) - b. \tag{4}$$

In our case, we have three classes, clumped, good, and sparse working areas. We employ the one-against-others method to form three 2-class SVMs for each pair of features. The maximum voting of the three is used to find the final classification results. During the training phase, the models of the three SVMs are learned from training data. In the testing phase, the learned models are employed to generate three sets of predictions for each test sample x. The one having the largest prediction is the final decision.

V. Experimental Results and Discussion

For convenience, Table I summarizes the aforementioned elementary features and their descriptions. From these features and their combinations, we choose the best performing set of features in the image classification validation experiments. We also discuss the classification benefits of the features.

TABLE I
Elementary Features and Their Descriptions.

Feature	Description
α_j^k	Spatial occupancy in block B_j^k
α	Occupancy or the mean of α_j^k at $k = 0$
σ_k	Standard derivation of all occupancies at level k
η	Total cell area/total perimeter of cell regions
λ	$\lambda = \sum_{k=1}^{K} \sigma_k^2 / K$
τ	$\tau = \sum_{k=1}^{K} \sigma_k$
n_c	Total number of cells per image
n_b	Total number of objects per image
γ	$\gamma = n_c / n_b$
e	Entropy, $e = -\sum p_A \log p_A$

A. Feature spatial distributions across one slide

To select appropriate features, it would be instructive to see the changes in feature values across the images of one slide moving from the "C" areas to the "G" areas and finally to the "S" areas. To visualize the changes, we choose a rectangular region from one slide containing 52×95 images and illustrate the two-dimensional spatial distribution of each feature in a 52×95 gray value image (Fig. 5). The brighter the pixel in the gray image, the larger the feature value is at the pixel. For comparison, we label "S", "G" and "C" images by 1, 2 and 3, respectively. The purpose of this labeling is to differentiate easily the classes of the images in the slide such that, when visualizing each label as a gray level pixel in a figure, there are three different levels of displaying brightness, namely, the darkest level (for "S" images), the moderately bright level (for "G" images) and the brightest level (for "C" images). We show the class labels in the top left panel in Fig. 5 for comparison. The border of each panel is highlighted in red. A visual inspection will give us some idea of the suitability of individual features to represent different classes of images. For example, α and σ_8 separate "S" images from "G" and "C" images, e performs well in identifying "G" images, and λ and τ can be used to classify the three classes. Features σ_1 and η are not able to separate "G" and "C" but they can be used to detect "S" images. The feature γ seems to have a low discrimination power.

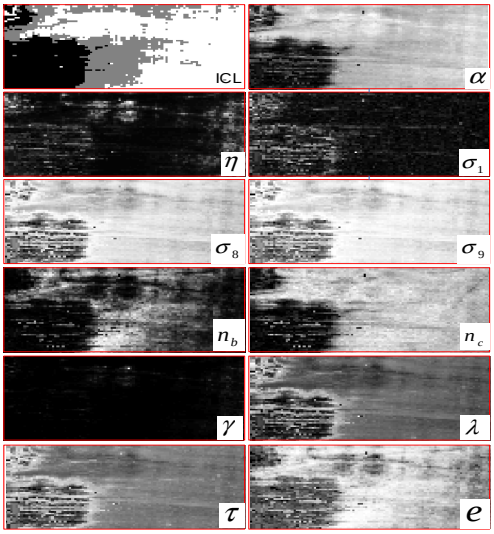

Fig. 5. Feature spatial distributions across the images of one slide. The top-left panel indicates the image class labels (ICL) with the brightest pixels corresponding to clumped images, the darkest pixels to sparse images, and the moderately bright pixels to good images. In the 11 other panels for α, η, σ_1, σ_8, σ_9, n_b, n_c, γ, λ, τ and e, the brighter the pixel, the larger the feature value.

B. Evaluation metrics

Before we discuss the details, we introduce the metrics to evaluate classification performance. For $n-$class problems, these are derived from an $n \times n$ *confusion matrix* $\mathbf{C}_n$ [26], whose entries $c_n(i, j)$, $i, j = 1, \ldots, n$, is the number of instances predicted as class i but actually belonging to class j. The GWA detection problem can be

considered a two-class classification problem that distinguishes "G" areas from "C" and "S" areas. Hence, we define [26], [27] sensitivity (or true positive rate) as SE $= c_2(1,1)/(c_2(1,1)+c_2(2,1))$, specificity (or true negative rate) as SP $= c_2(2,2)/(c_2(1,2)+c_2(2,2))$, positive predictive value as PPV $= c_2(1,1)/(c_2(1,1)+c_2(1,2))$ and negative predictive value as NPV $= c_2(2,2)/(c_2(2,1)+c_2(2,2))$. If the four measures SE, SP, PPV, and NPV are high simultaneously for a classifier, then the classification is good. We thus hope that their mean value, $\hat{\mu}$, is high while their variance, $\hat{\sigma}$, is low. $\hat{\mu}$ is thus considered as the major performance index. For the classification of "C", "G" and "S", we define, from the confusion matrix $\mathbf{C}_3$, the hit rate for each class j,

$$h_j = c_3(j,j)/\sum_{i=1}^{3} c_3(i,j), j = 1,2,3. \quad (5)$$

In particular, we denote $h_g = h_1$, $h_c = h_2$ and $h_s = h_3$, for class "G", "C", and "S", respectively. The total misclassification rate is given by

$$\varepsilon = \frac{\sum_{i=1}^{3}\sum_{j=1}^{3} c_3(i,j) - \sum_{i=1}^{3} c_3(i,i)}{\sum_{i=1}^{3}\sum_{j=1}^{3} c_3(i,j)}. \quad (6)$$

C. Experimental setup

The computation platform is a Xeon 3.6GHz CPU with 2GB RAM using Matlab 7.4 calling SVM*Torch* [28] executables compiled in C++. We use the linear kernel and set $C = 100$ in SVM. More than 15000 images are taken from four malaria-infected Giemsa-stained blood smears using an oil immersion $100\times$ objective and a $10\times$ ocular with a digital camera (Pixelink PL-A662) linked to a motorized microscope (Olympus BX51). We use a 10-level pyramid with $K = 9$ for multi-scale image representation. From these images, experts selected and marked some images for the three classes ("C", "G" and "S"). In the experiments, the training data are first normalized to $[0,1]$. The test data are then transformed accordingly.

We use 20 images for each class from one slide for training. For feature selection and performance comparison, the test images are from dataset D1 (41 from "C", 48 from "G", and 45 from "S"). Then, we include 128 extra images to form a new dataset D2 and examine the robustness of our method. Finally, another dataset D3 (2494 from "C", 1316 from "G", 1068 from "S") from another slide are tested.

We first combine the features to form a higher-dimensional feature space in SVM. We evaluate 50 distinct combinations of features and test them on different data sets. These experiments are indexed by an item number x ($\#x$). The first 47 combinations are tested on D1. The performance metrics of the 47 experiments are summarized numerically in Tables II (for #1 to #20) and III (for #21 to #47). The remaining three of the 50 combinations of features are however tested not only on D1, but also on D2 and D3. The nine sets of experiments are indexed from #48 to #56 with their performance metrics compared in Table IV. In Fig. 6 we show an error bar plot for all experiments indexed by their item numbers, where each $\hat{\mu}$ is marked by a cross (x) and the corresponding $\hat{\sigma}$ is the half length of the vertical bar located symmetrically above and below $\hat{\mu}$.

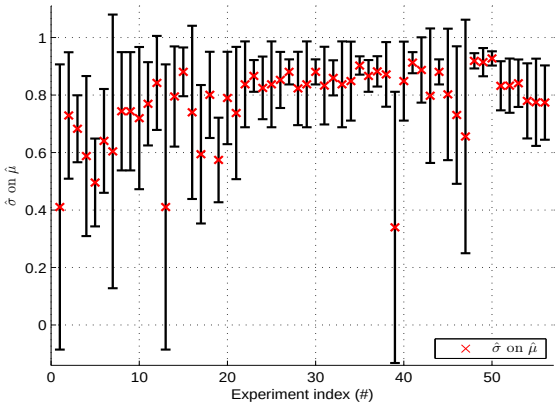

Fig. 6. An error bar plot for all experiments: each $\hat{\mu}$ is marked by a cross (x) and the corresponding $\hat{\sigma}$ is the half length of the vertical bar locating symmetrically above and below $\hat{\mu}$.

D. Results after feature selection

Actually, features σ_k, $k = 1,..K$, at different scales, perform differently in image classification. As seen in Table II, σ_8 and σ_9 perform better than σ_1, σ_2, ..., σ_7 while σ_1 has a poor hit rate for class "G". Hence, σ_8 is preferred to separate "S" and "G", and σ_9 to separate "C" and "G". We choose σ_8 for further feature fusion in GWA classification.

In Table II, we also compare the performances of $\#10$ to $\#20$ using σ_1 and/or σ_8. Generally, feature combinations using σ_8 perform better than those using σ_1. For example, the feature pair (η, σ_8) outperforms (η, σ_1) in the detection of "G" as the hit rate h_g of (η, σ_8) is higher than that of (η, σ_1). (α, η, σ_8) is also better than (α, η, σ_1).

TABLE II
PERFORMANCE (%) COMPARISONS: BENEFITS FROM σ_8 AND λ.

#	Feature(s)	SE	SP	h_g	h_c	h_s	ε
1	σ_1	0.0	100.0	0.0	0.0	100.0	69.4
2	σ_2	91.7	54.7	91.7	0.0	97.6	37.3
3	σ_3	72.9	65.1	72.9	13.3	100.0	38.8
4	σ_4	22.9	89.5	22.9	55.6	97.6	43.3
5	σ_5	37.5	61.6	37.5	6.7	26.8	76.1
6	σ_6	41.7	83.7	41.7	11.1	48.8	66.4
7	σ_7	100	4.7	100.0	0.0	9.8	61.2
8	σ_8	91.7	58.1	91.7	0.0	65.9	47.0
9	σ_9	91.7	58.1	91.7	51.1	0.0	50.0
10	α, σ_1	37.5	95.3	37.5	91.1	100.0	25.4
11	η, σ_1	87.5	68.6	87.5	44.4	65.9	33.6
12	α, η, σ_1	97.9	73.3	97.9	53.3	95.1	17.9
13	α, σ_8	0.0	100.0	0.0	100.0	65.9	46.3
14	σ_8, η	93.8	67.4	93.8	35.6	61	35.8
15	α, σ_8, η	93.8	84.9	93.8	71.1	100.0	11.9
16	η	100.0	45.3	100.0	42.2	0.0	50.0
17	λ	29.2	86	29.2	20.0	48.8	67.9
18	σ_8, λ	91.7	70.9	91.7	42.2	100.0	22.4
19	τ	43.8	70.9	43.8	48.9	24.4	60.4
20	σ_8, τ	91.7	68.6	91.7	37.8	100.0	23.9

E. Performance benefits using defined features

The features that we have defined, namely, the number of objects n_b, the entropy e and the number of cells n_c in the image have different functionalities in classification.

This subsection discusses their performance benefits as well as the best performing feature combinations. Previously, we had regarded objects as collections of pixels and benchmarked the classification using pixel-based features. Here, we directly count the number of objects. Since cells have finite sizes, the number of non-overlapping cells must be constrained within a certain range. Hence, n_b measures the clumping degree implicitly.

In Table III, experiments $\#21$ to $\#28$ are used to show performance improvements introduced by n_b. The improvement in GWA classification due to n_b can be seen. Although α and n_b have similar $\hat{\mu}$ and $\hat{\sigma}$, α is good at detecting classes "C" and "S" while n_b has good discriminative ability in detecting class "G". They appear to complement each other. Hence, the feature combination of α and n_b will produce better results than α or n_b alone. Since n_b and σ_8 have similar hit and miss rates for the three classes, either of them or their combination should result in almost the same performance. This explains the observation that the feature combination (α, n_b) performs well but slightly worse than (α, σ_8, n_b). The best feature combination is (α, σ_8, n_b) with $\hat{\mu}$ and $\hat{\sigma}$ equal to 88.0% and 4.4%, respectively. The hit rates are above 80.0% and the total misclassification rate is 11.2%.

TABLE III
PERFORMANCE (%) COMPARISONS: BENEFITS FROM n_b, e AND n_c.

#	Feature(s)	SE	SP	h_g	h_c	h_s	ε
21	α	41.7	95.3	41.7	91.1	100.0	23.9
22	n_b	95.8	74.4	95.8	13.3	80.5	36.6
23	α, n_b	87.5	87.2	87.5	75.6	100.0	12.7
24	σ_8, n_b	89.6	77.9	89.6	53.3	51.2	34.3
25	n_b, η	95.8	74.4	95.8	33.3	87.8	27.6
26	n_b, λ	91.7	81.4	91.7	33.3	48.8	41.0
27	α, σ_8, n_b	87.5	89.5	87.5	80.0	100.0	11.2
28	σ_8, n_b, η	91.7	75.6	91.7	46.7	63.4	32.1
29	e	95.8	74.4	95.8	37.8	68.3	32.1
30	α, e	87.5	89.5	87.5	80.0	100.0	11.2
31	σ_8, e	93.8	75.6	93.8	48.9	53.7	33.6
32	n_b, e	87.5	86.0	87.5	73.3	43.9	30.6
33	η, e	95.8	74.4	95.8	35.6	87.8	26.9
34	λ, e	95.8	76.7	95.8	40.0	68.3	31.3
35	α, σ_8, e	87.5	93	87.5	86.7	100.0	9.0
36	α, n_b, e	87.5	87.2	87.5	75.6	100.0	12.7
37	α, η, e	89.6	88.4	89.6	77.8	100.0	11.2
38	α, n_c	95.8	81.4	95.8	64.4	100.0	13.4
39	σ_8, n_c	100.0	0.0	100.0	0.0	0.0	64.2
40	n_c, η	95.8	76.7	95.8	55.6	97.6	17.2
41	α, σ_8, n_c	91.7	91.9	91.7	84.4	100.0	8.2
42	σ_8, n_c, η	97.9	82.6	97.9	66.7	97.6	12.7
43	n_c, λ	100.0	60.5	100.0	22.2	100.0	26.1
44	n_c, e	87.5	89.5	87.5	80.0	100.0	11.2
45	n_c, τ	100.0	61.6	100.0	24.4	100.0	25.4
46	n_c, σ_1	93.8	52.3	93.8	17.8	87.8	33.6
47	n_c	100.0	20.9	100.0	0.0	43.9	50.7

Experiments $\#29$ to $\#37$ in Table III involve the entropy e. Comparing these results, we see clear improvements obtained by introducing e. Entropy is especially good at GWA detection (with a hit rate 95.8% for class "G"). Very good performances are obtained by combining α and e and also by combining e with other features. For the feature combination (α, σ_8, e), all hits are above 86.7% and the misclassification rate is 9.0%. For the detection of GWAs, we achieve $\hat{\mu}$ of 90.3% and $\hat{\sigma}$ 3.2%, respectively.

We have proposed the total cell count n_c for GWA classification. The count n_c is an explicit quantification of cell clumping, just as n_b is. However, n_c is more effective in discriminating different working areas. The quantitative results involving n_c are detailed in $\#38$ to $\#47$ in Table III. Comparing #21 (α, SE =41.7%, SP=95.3%) and #47 (n_c, SE=100.0%, SP=20.9%), we find that they are complementary in SE and SP. Hence the number of cells per object and the object area are two different factors in measuring the degree of cell clumping in the object. By using them together in #38 (α, n_c), we obtain high values of both SE (95.8%) and SP (81.4%). The combination (α, σ_8, n_c) works very well with $\hat{\mu} = 91.3\%$ which is the highest so far we have achieved for 3-feature combinations. The variance $\hat{\sigma} = 3.7\%$ is also the lowest. For (α, σ_8, n_c), the hits are better than 84.4% and the total misclassification rate is 8.2%.

F. Results for large datasets and computational time

We can generally achieve better performances when more features are combined. However, it does not mean that using all features will present the best result. Using dataset D1, the three top performing feature combinations are #48 $(\alpha, \sigma_8, \lambda, e)$, #49 $(\alpha, \sigma_8, \eta, \gamma, \tau)$ and #50 $(\alpha, \sigma_8, n_c, \eta, \lambda, e)$ (see Table IV for details). To further check the robustness of our method, we conducted two sets of experiments using the same feature sets with #48, #49 and #50 but tested on datasets D2 ($\#51$, $\#52$ and $\#53$) and D3 ($\#54$, $\#55$ and $\#56$), respectively. The results are presented in Table IV as well. Comparing their corresponding performance metrics, we observe a decrease in performance when more data are tested. However, we notice that such a decrease is not significant, especially for class "G", in the sense that, for the tested 4878 images from a slide different from those used for training, the hit rates for "C", "G" and "S" are still above 78.1%, with the sensitivity and the specificity above 80.0% as well.

Finally, it took, on average, less than 5 seconds for all pre-classification steps, including image processing and feature extraction for each image. In addition, both training and testing using SVMs for each classification took less than 5 seconds.

TABLE IV
PERFORMANCE (%) COMPARISONS: DIFFERENT DATASETS.

#	$\hat{\mu}$	$\hat{\sigma}$	SE	SP	h_g	h_c	h_s	ε
48	91.9	2.7	89.6	94.2	89.6	88.9	100.0	7.5
49	91.4	4.9	93.8	90.7	93.8	82.2	100	8.2
50	**92.7**	**2.5**	91.7	94.2	91.7	88.9	100	6.7
51	83.2	8.6	81.6	87.1	81.6	70.4	98.1	15.3
52	83.3	9.4	84.2	85.5	84.2	66.7	97.1	16.0
53	**84.1**	**8.2**	82.9	87.6	82.9	70.4	97.1	15.3
54	78.0	13.1	79.8	80.4	79.8	71.3	97.0	20.8
55	77.5	15.2	83.6	76.6	83.6	66.0	96.2	22.7
56	77.4	12.9	78.1	80.6	78.1	71.4	94.8	21.7

VI. CONCLUSION

The automatic detection of suitable working regions and classifying different types of regions in peripheral blood

smears have several advantages for later detailed cell enumeration and diagnosis, in particular, improving the consistency in identifying regions; broadening the inspection region range from around ten to a few hundred images depending on the actual sample size; reducing statistical bias for diagnosis based on more region samples; and facilitating subsequent automatic high throughput screening and telepathology applications.

We have reported promising results in 2008 [8], [10]. The present paper extends our previous work by not only providing comprehensive details but also including new methods with improved performances. We have adopted an efficient algorithm to split clumped cells. As the current objective is to use GWA detection as a preprocessing step before further detailed cell analysis in the context of high throughput screening, an efficient area selection is desired, instead of an accurate but computationally more expensive method for very accurate cell segmentation. Furthermore, our primary concern is to measure the goodness of GWAs, such as the degree of clumping and cell spatial distributions. The method combines the erosion-based technique and the watershed technique for cell clump splitting, which is efficient and accurate enough for image classification.

We have shown that the area of a clump and the number of cells it contains are different features quantifying the degree of clumping. We can achieve better sensitivity and specificity in classifying images by using both features at the same time. We have demonstrated that entropy e as a collective measure for the occurrence frequency of differently sized objects in an image can be used to improve the detection of GWAs. We have also shown that, the cell spatial spreading quantified by using σ_8 and λ is also helpful to improve classification performance. Our results show that the top performing combinations of features normally involve these elementary features.

Extensive validations have been done on 60 training images and 134 other test images. We have obtained ($\hat{\mu}$,$\hat{\sigma}$) to be (92.7% , 2.5%), and 91.7% sensitivity and 94.2% specificity for GWA detection, with all hit rates better than 88.9% and a total misclassification rate 6.7% for the three classes. Finally, we have tested the method on a test set of 4878 images and achieved above 78.1% hit rates, demonstrating acceptable robustness of the current work. In a Matlab implementation, it took less than 5 seconds for image analysis and less than 5 seconds for each classification, respectively. This lays the foundation for efficient GWA detection as a preprocessing step in high throughput microscope screening.

ACKNOWLEDGMENT

The authors would like to thank the two anonymous reviewers who made constructive comments which helped improve the current paper.

REFERENCES

[1] G. L. Voigt, *Hematology Techniques and Concepts for Veterinary Technicians*. Blackwell Publishing, 2000.

[2] C. E. Mutschler and M. E. Warner, "Pattern recognition system with working area detection," U.S. Patent 4702595, 1987.

[3] R. Wollman and N. Stuurman, "High throughput microscopy: From raw images to discoveries," *Journal of Cell Science*, vol. 120, no. 21, pp. 3712–3722, 2007.

[4] P. N. Furness and W. M. Bamford, "Telepathology," *Current Diagnostic Pathology*, vol. 7, no. 4, pp. 281–291, 2001.

[5] M. Ingram, P. Norgren, and K. Preston, "Automatic differentiation of white blood cells," in *Image Processing in Biological Science (UCLA Forum in Medical Science 9)*, D. M. Ramsey, Ed. University of California Press, 1968.

[6] J. Angulo and G. Flandrin, "Automated detection of working area of peripheral blood smears using mathematical morphology," *Analytical Cellular Pathology*, vol. 25, no. 1, pp. 37–49, 2003.

[7] J. V. Dacie and S. M. Lewis, *Practical Haematology*. London: Churchill Ltd., 1963.

[8] W. Xiong, J. H. Lim, S. H. Ong, N. N. Tung, J. Liu, D. Racoceanu, K. Tan, A. Chong, and K. Foong, "Automatic working area classification on peripheral blood smears without cell central zone extraction," in *Proceedings of the 30th IEEE Conference Engineering in Medicine and Biology Society*, Vancouver, British Columbia, Canada, August 2008, pp. 4074–4077.

[9] L. Ballerini, "A simple method to measure homogeneity of fat distribution in meat," in *Proceedings of the 12th Scandinavian Conference on Image Analysis*, Bergen, Norway, June 2001, pp. 343–349.

[10] W. Xiong, S. H. Ong, J. H. Lim, N. N. Tung, J. Liu, D. Racoceanu, K. Tan, A. Chong, and K. Foong, "Automatic working area classification in peripheral blood smears using spatial distribution features across scales," in *Proceedings of the 19th International Conference on Pattern Recognition*, Tampa, Florida, USA, December 2008, pp. 1–4.

[11] N. Otsu, "A threshold selection method from gray-level histograms," *IEEE Transactions on Systems, Man and Cybernetics*, vol. 9, no. 1, pp. 62–66, 1979.

[12] S. H. Ong, Jayasooriah, H. H. Yeow, and R. Sinniah, "Decomposition of digital clumps into convex parts by contour tracing and labeling," *Pattern Recognition Letter*, vol. 13, no. 11, pp. 789–795, November 1992.

[13] S. Beucher and C. Lantuejoul, "Use of watersheds in contour detection," in *Proceedings of the 1979 International Workshop on Image Processing, Real-Time Edge and Motion Detection/ Estimation*, Rennes, France, September 1979, pp. 17–21.

[14] G. Cong and B. Parvin, "Model-based segmentation of nuclei," *Pattern Recognition*, vol. 33, no. 8, pp. 1383–1393, 2000.

[15] J. E. Bowie and I. T. Young, "An analysis technique for biological shape–ii," *Acta Cytologica*, vol. 21, no. 3, pp. 455–464, 1977.

[16] T. T. E. Yeo, X. C. Jin, S. H. Ong, Jayasooriah, and R. Sinniah, "Clump splitting through concavity analysis," *Pattern Recognition Letter*, vol. 15, no. 10, pp. 1013–1018, 1994.

[17] S. Kumar, S. H. Ong, S. Ranganath, T. C. Ong, and F. T. Chew, "A rule-based approach for robust clump splitting," *Pattern Recognition*, vol. 39, no. 6, pp. 1088–1098, 2006.

[18] F. Meyer, "Topographic distance and watershed lines," *Signal Processing*, vol. 38, no. 1, pp. 113–125, July 1994.

[19] N. Yokoya and S. Araki, "A new splitting active contour model based on crossing detection," in *Proceedings of the 2nd Asian Conference on Computer Vision*, Singapore, December 1995, pp. 346–350.

[20] H. H. S. Ip and R. P. K. Yu, "Recursive splitting of active contours in multiple clump segmentation," *Electronics Letter*, vol. 32, no. 17, pp. 1564–1566, 1996.

[21] P. Soille, *Morphological Image Analysis: Principles and Applications*, 2nd ed. Springer-Verlag New York, Inc., 2003.

[22] J. C. Russ, *The Image Processing Handbook*, 2nd ed. CRC Press, Inc, 1995.

[23] J.-O. Johansson, "Measuring homogeneity of planar point-patterns by using kurtosis," *Pattern Recognition Letters*, vol. 21, no. 13, pp. 1149–1156, 2000.

[24] H. D. Cheng, M. Xue, and X. J. Shi, "Contrast enhancement based on a novel homogeneity measurement," *Pattern Recognition*, vol. 36, no. 11, pp. 2687– 2697, 2003.

[25] G. S. Haykin, *Neural Networks: A Comprehensive Foundation*, 2nd ed. Prentice Hall, 1999.

[26] R. Kohavi and F. Provost, "Glossary of terms," *Machine Learning*, vol. 30, no. 2-3, pp. 271–274, 1998.

[27] D. G. Altman and J. M. Bland, "Diagnostic tests 2: Predictive value," *British Medical Journal (Clinical Research Edition)*, vol. 309, no. 6947, pp. 102–105, July 1994.

[28] R. Collobert, S. Bengio, and C. Williamson, "SVMTorch: Support vector machines for large-scale regression problems," *Journal of Machine Learning Research*, vol. 1, pp. 143–160, 2001.

Wei Xiong (M'09) received the B.E. degree from Huazhong University of Science and Technology, Wuhan, China, and the M.Sc. (by research) degree from the National University of Singapore (NUS), Singapore, where he is currently working toward the Ph.D. degree.

He is currently with Institute for Infocomm Research (I2R), Agency for Science, Technology and Research (A*STAR), Singapore. He was with the Chinese Academy of Sciences from 1988 to 1999 before joining I2R, in 2000. His current research interests include computer vision, pattern recognition, and content-based image retrieval in biomedical domains. He has authored or coauthored more than 40 publications in peer-reviewed international journals and conference proceedings.

Sim-Heng Ong (S'80-M'84) received the B.E. (Hons.) degree from the University of Western Australia, Perth, W.A., Australia, and the Ph.D. degree from the University of Sydney, Sydney, N.S.W., Australia.

He is currently an Associate Professor jointly in the Department of Electrical Engineering and the Division of Bioengineering, National University of Singapore, Singapore. His current research interests include computer vision and biomedical image processing. He has authored or coauthored more than 250 papers published in international journals and conference proceedings.

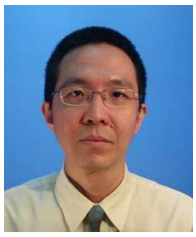

Joo-Hwee Lim (M'07) received the B.Sc. (Hons I) and M.Sc. (by research) degrees in Computer Science from the National University of Singapore and the Ph.D. degree in Computer Science and Engineering from the University of New South Wales, Sydney, N.S.W., Australia.

He is currently the Head of the Computer Vision and Image Understanding Department, Institute for Infocomm Research (I2R), Agency for Science, Technology and Research (A*STAR), Singapore. He is also the co-Director of the Image and Pervasive Access Laboratory (IPAL), a French-Singapore Joint Lab (UMI 2955, January 2007 to December 2010) and the Director (Imaging) of a new joint laboratory SAILOR (June 2009 to June 2012) between I2R and Singapore Eye Research Institute, where computer scientists and clinicians collaborate closely. He has authored or coauthored more than 140 international refereed journal and conference papers and co-authored 15 patents (awarded and pending) in his research areas such as pattern recognition, image understanding and medical image analysis.

Kelvin Foong Weng Chiong (BDS, MDS, M OrthRCSEd, FAMS, FDS RCSEd, PhD) is a specialist dental surgeon. He graduated from the National University of Singapore with the dental degree in 1988, and received speciality training at The University of Adelaide from 1992-1994. He received his PhD in 2005, having studied the topic of 3D surface imaging of cleft palate deformity in infants.

He is currently an Associate Professor in the Faculty of Dentistry, National University of Singapore. He also holds the appointment of Senior Consultant in Orthodontics at the National University Hospital. His current research interests include the application of 3-D image processing and visualization techniques for the development of accurate, patient-specific virtual models of the teeth, face and head. He works in close collaboration with research partners in the fields of Vision Engineering and Image Processing to develop virtual models of the face and teeth.

Jiang Liu graduated from the University of Science and Technology of China, Hefei, China, and the School of Computing, National University of Singapore, Singapore.

During the past 22 years, he had worked for industries holding technical development and management positions. In the past six years, he has focused his research on medical imaging. He is the leader of the Feature and Segmentation Group and the Intelligent Medical Imaging (iMED) team, Institute for Infocomm Research (I2R), Agency for Science, Technology and Research (A*STAR), Singapore. He is currently engaged in computed tomography (CT), retina image processing as well as medical-image-based computer-assisted diagnosis (CAD)/computer aided surgery (CAS). He is an adjunct Research Scientist in Singapore Eye Research Institute, Singapore General Hospital.

Daniel Racoceanu (M'06) received the M.Eng. degree in mechatronics from the "Politehnica" University of Timisoara, Timisoara, Romania, in 1992, the M.Sc. degree in automatics and industrial informatics from the University of Technology of Belfort-Montbéliard (UTBM), Belfort, France, in 1993, the Ph.D. degree in 1997 and Habil-Dr. degree in 2006 in control and computer sciences from the University of Besançon, Besançon, France.

He was a Project Manager at General Electric Energy Products - Europe, Belfort, France. In 1999, he was an Associate Professor at the Faculty of Sciences of the University of Besançon, where he was engaged in the field of artificial intelligence, computer vision, industrial informatics, automation, control science and production systems. He is currently a Senior Scientist at the French National Research Center (CNRS) and the Director (France) of the Image and Pervasive Access Lab (IPAL), the International Joint Research Unit (UMI CNRS 2955) created in Singapore between the CNRS, the National University of Singapore (NUS), the Institute for Infocomm Research (I2R), Agency for Science, Technology and Research (A*STAR), Singapore, and the University Joseph Fourier of Grenoble (UJF), France. At IPAL, he is involved in intelligent diagnosis/prognosis assistance using medical image and knowledge-based reasoning systems, content and context based medical image retrieval and medical multimedia fusion. Since November 2009, he has been an adjunct Associate Professor at the National University of Singapore.

Alvin G. L. Chong is currently a postgraduate student in the Department of Microbiology, National University of Singapore, Singapore.

Kevin S. W. Tan received the Ph.D. from the Department of Microbiology, National University of Singapore, Singapore.

He is currently with the Department of Microbiology, National University of Singapore. He was a Postdoctoral Fellow in the Laboratory of Molecular Parasitology, The Rockefeller University. He is engaged in researches on protozoan cell death focusing on PCD pathways in the enteric parasite blastocystis and the malaria parasite Plasmodium falciparum. He is a member of the Singapore MIT-Alliance for Research and Technologies Interdisciplinary Research Group on Infectious Diseases (SMART IRG ID), and his project is aimed at investigating the biomechanical aspects of malaria cell death. His current research interests include hostCpathogen interactions, molecular mimicry, and nanotechnological tools.